RSC Advances

PAPER

View Article Online
View Journal | View Issue

Cite this: *RSC Adv.*, 2025, **15**, 47271

Rationally designed In–CeO_2/g-C_3N_4 S-scheme heterojunction photocatalyst with tuned redox ability for the photocatalytic degradation of pharmaceutical contaminants

Mazen R. Alrahili,[a] Mohamed Abdel Rafea,[b] Magdi E. A. Zaki,[c] M. Khairy,[c] Mohamed R. El-Aassar,[d] Sultan Albarakati,[e] Imran Shakir,[f] Abdullah K. Alanazi[g] and Muhammad Aadil[*h]

Herein, the synthesis of an indium-doped cerium oxide/graphitic carbon nitride (In–CeO_2/g-C_3N_4) S-scheme heterojunction aimed at optimizing photocatalytic degradation under visible light for the remediation of pharmaceutical wastewater is reported. The materials were synthesized *via* a hydrothermal process, in which pure CeO_2 and In-modified CeO_2 (In–CeO_2) were initially synthesized, followed by the incorporation of g-C_3N_4 to produce the heterojunction. A series of characterization methods, such as X-ray diffraction (XRD), Fourier-transform infrared spectroscopy (FTIR), thermogravimetric analysis (TGA), and scanning electron microscopy (SEM), validated the effective synthesis and structural integrity of CeO_2, In–CeO_2, and In–CeO_2/g-C_3N_4. The optical bandgap of the samples was determined, presenting a reduction from 2.97 eV for CeO_2 to 2.69 eV for In–CeO_2/g-C_3N_4, which facilitated better visible-light absorption. Photocurrent and electrochemical impedance spectroscopy (EIS) characterizations indicated enhanced charge separation and reduced recombination in the In–CeO_2/g-C_3N_4 heterojunction. Photocatalytic experiments for the degradation of levofloxacin (LVX) demonstrated that the In–CeO_2/g-C_3N_4 heterojunction achieved 85% degradation, significantly higher than those achieved by In–CeO_2 (63%) and CeO_2 (44%), highlighting the enhanced photocatalytic performance of the heterojunction. The higher photocatalytic activity is attributed to the formation of an S-scheme charge migration channel, enabling efficient charge separation. Results indicate that the In–CeO_2/g-C_3N_4 heterojunction has great potential for water purification applications, particularly in degrading drug contaminants.

Received 16th September 2025
Accepted 17th November 2025

DOI: 10.1039/d5ra07023f

rsc.li/rsc-advances

1. Introduction

Utilizing visible light for the photocatalytic degradation of organic pollutants is an economical and sustainable cleantech solution to the escalating environmental pollution and water contamination.[1,2] Despite its promise, the development of photocatalysts is a challenging process because the conventional semiconductor materials, including TiO_2,[3,4] ZnO,[5,6] and CeO_2,[7,8] have low quantum efficiency due to their electronic band structures (wide optical bandgaps), which prevent harnessing the visible part (∼43%) of solar light, and their photogenerated charge carriers (electron–hole pairs) recombine rapidly limiting their availability.[9–11]

Cerium oxide (CeO_2), commonly known as ceria, is an emerging material in the realm of photocatalysts, which is resistant to photocorrosion and is chemically and thermally stable.[12,13] The applicability of ceria as a promising photocatalyst is explicitly limited by its weak visible-light activity and high electron–hole pair recombination, which are crucial factors for visible-light-driven photocatalysis.[14–16] Several investigations, including metal-doping, indicate that cerium oxide modification tunes the electronic structure and enhances the quantum efficiency.[16–19] The rapid electron–hole recombination can be suppressed by coupling ceria with another photocatalytic material through the formation of heterostructure junctions, thereby increasing the availability of charge carriers for photocatalytic reactions.[20–23]

[a]Department of Physics, College of Science, Taibah University, Madinah, Saudi Arabia
[b]Department of Physics, College of Science, Imam Mohammad Ibn Saud Islamic University (IMSIU), 11623 Riyadh, Saudi Arabia
[c]Department of Chemistry, College of Science, Imam Mohammad Ibn Saud Islamic University (IMSIU), Riyadh, 11623, Saudi Arabia
[d]Department of Chemistry, College of Science, Jouf University, PO Box 2014, Sakaka, Aljouf, Saudi Arabia
[e]Department of Physics, College of Science, University of Jeddah, Jeddah, Saudi Arabia
[f]Department of Physics, Faculty of Science, Islamic University of Madinah, Madinah 42351, Saudi Arabia
[g]Department of Chemistry, College of Science, Taif University, Taif, Saudi Arabia
[h]Department of Chemistry, Rahim Yar Khan Campus, The Islamia University of Bahawalpur, Rahim Yar Khan 64200, Pakistan. E-mail: Mhammad.aadil@iub.edu.pk

Assembling two different photocatalytic materials with distinct electronic properties to construct heterostructure junctions enhances charge separation, which is crucial for significant photocatalytic performance.[24–26] These materials possess distinct electronic band structures that facilitate the migration and separation of photogenerated electron–hole pairs, enhancing the photocatalytic performance.[27,28] For instance, S-scheme heterojunction formation involves the interfacial contact of two photocatalysts, in which band structure alignment results in the accumulation of holes in the valence band of one of the combining photocatalysts and electrons in the conduction band of the other photocatalyst, which is mainly compelled by the internal electric field.[29] Graphitic carbon nitride g-C_3N_4 (g-CN), a polymeric compound with a layered structure of tri-*s*-triazine units, exhibits high thermal and chemical stability with excellent visible-light activity. The distinguished properties, which include non-toxicity, a unique metal-free framework, and a semiconductor with a medium band gap, enable its use as a sustainable catalyst for photodegradation applications. Despite these characteristics, g-CN exhibits low quantum efficiency due to a low absorptivity coefficient and sluggish electron–hole separation, which can be improved by modifying g-CN. Various reports present g-CN as a promising material for the fabrication of heterostructure junctions, as its unique structural framework favours interfacial contact.[30,31] For instance, ZrO_2/g-CN,[32] $Ce(MoO_4)_2$/g-CN, g-CN/$Bi_2O_2CO_3$–Bi_4O_7,[33] Nd/Ni–$LaFeO_3$/g-CN,[34] $CdMoO_4$/g-CN,[35] ZnO/g-CN,[36] Ni-MOF/g-CN,[37] and ZnAl-LDH/g-CN[38] include the g-CN-based material designs for wastewater decontamination applications. The findings reveal that these composite designs not only increase the optical response but also facilitate charge separation and transport primarily through the formation of heterojunctions.

Based on the facts described above, we synthesized a visible-light-activated In–CeO_2/g-CN S-scheme heterojunction to facilitate charge separation and transport, thereby augmenting the effective photocatalytic removal of pharmaceutical pollutants. The hydrothermal method was used to synthesize pure CeO_2 and its indium-modified form, In–CeO_2, while melamine was calcinated for its thermal polymerization to prepare g-CN. Both the components, In–CeO_2 and g-CN, were subjected to ultrasonication to fabricate the In–CeO_2/g-CN heterojunction. The synthesized materials were characterized to investigate their crystal structure formation, thermal stability, microstructure, optical activity, and electrochemical response. The photocatalytic efficiency of In–CeO_2/g-CN was estimated by degrading levofloxacin, a typical pollutant, showcasing the effect of heterojunction formation on photocatalytic performance. The present work aims to significantly contribute to the design of heterojunction materials for the photocatalytic degradation of pharmaceutical contaminants in wastewater remediation.

2. Experimental

2.1 Chemicals

The chemicals, including ceric ammonium nitrate (Sigma-Aldrich, $(NH_4)_2[Ce(NO_3)_6]$, ≥ 98.5%), indium nitrate (Sigma-Aldrich, $In(NO_3)_3$, 99.99%), and melamine (Sigma-Aldrich, Powder, 99%), were used in the synthesis of CeO_2, In–CeO_2, and In–CeO_2/g-CN materials. Levofloxacin (LVX, $C_{18}H_{20}FN_3O_4$), ethylenediaminetetraacetic disodium salt (Sigma-Aldrich, EDTA-2Na, 99%), silver nitrate (AgNO3), isopropyl alcohol (Sigma-Aldrich, IPA, 99%), and benzoquinone (Sigma-Aldrich, BZQ, 99%) were used in the photocatalytic activity investigation. All the standards were prepared in DI water ($k < 6\ \mu S\ cm^{-1}$).

2.2 CeO_2 and In–CeO_2 synthesis

The facile hydrothermal method was applied to synthesize pure CeO_2 and In–CeO_2 materials. Initially, 3 g of $(NH_4)_2[Ce(NO_3)_6]$ was added to 70 mL of DI water while stirring until the formation of a clear solution, followed by the addition of 0.15 g $In(NO_3)_3$. The pH was raised to ∼10 with drop-by-drop addition of NH_4OH, and the solution was poured into a Teflon cup enclosed in an autoclave (stainless steel-made), following the heating of the solution at 180 °C for 12 h. The precipitates collected were thoroughly washed with DI water multiple times to neutralize the pH and remove unreacted precursors, and then dried at 55 °C for 2 h.

2.3 Preparation of g-CN powder

The g-CN powder was prepared from melamine through thermal condensation.[39] Experimentally, 2 g of the precursor powder was placed in a 25 cc (porcelain) crucible and heated at 550 °C for 6 h at 5 °C min^{-1}. Upon the completion of the heating process, the crucible was removed from the furnace and allowed to cool naturally in the air. The pale, yellowish-colored g-CN formed was collected and stored in a dry environment.

2.4 In–CeO_2/g-CN construction

The g-CN-based heterojunction of modified In–CeO_2 was formed using an ultrasonication method. In the experiment, 0.9 g of In–CeO_2 was poured into DI water (100 mL) and sonicated with an ultrasonic probe for 1 hour. Similarly, in a beaker (100 mL, DI water), 0.1 g of g-CN powder was separately sonicated. The resulting suspensions were mixed, followed by sonication again for 1 hour to enhance the interaction and dispersion of In–CeO_2 with g-CN, assembling the In–CeO_2/g-CN heterojunction (Fig. 1).

2.5 Characterization

The crystal structure formation and phase purity of the fabricated materials were investigated by powder XRD (X-ray Diffractometer, Shimadzu 6100 AS, Cu-Kα radiation, $\lambda = 0.154$ nm) and FTIR spectroscopy (Shimadzu IRAffinity-1S Spectrophotometer), while for thermal stability, TGA (Thermo Plus Evo, TG8120 Rigaku) was performed. The morphology was explored by SEM (Scanning electron microscope, FEI S50) and optical activity by UV-vis spectroscopy (Double-Beam Spectrophotometer, Jenway/6850). The electrochemical response was recorded on a three-electrode potentiostat (reference electrode = Ag/AgCl, working electrode = indium tin oxide-coated glass, and

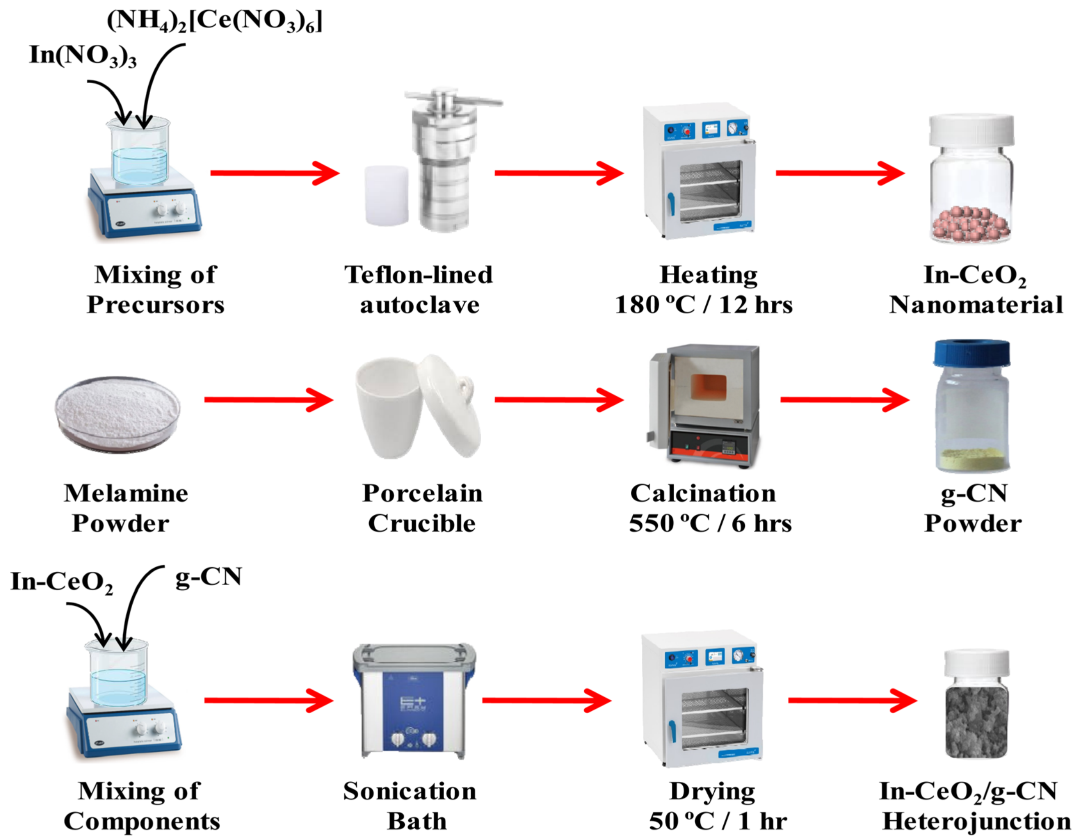

Fig. 1 Schematic of the synthesis of CeO_2 and In–CeO_2 (hydrothermal), g-CN (calcination), and In–CeO_2/g-CN (ultrasonication).

auxiliary electrode = Pt wire) in 1 M Na_2SO_4 electrolytic solution.

2.6 Photocatalytic (PC) efficiency

The PC efficiency of CeO_2, In–CeO_2, and In–CeO_2/g-CN photocatalysts was evaluated by degrading LVX under a Xe lamp (300 W, UV cutoff filter λ > 420 nm) placed 20 cm above the reaction mixture. Initially, 0.05 g of CeO_2, In–CeO_2, and In–CeO_2/g-CN were dispersed in LVX (10 mg L^{-1}, 100 mL) solutions in three separate beakers. The resultant mixtures (LVX + photocatalyst) were kept in the dark and stirred for 40 minutes to acquire LVX adsorption–desorption equilibria on the catalyst surface. Afterward, the solutions were exposed to light to initiate LVX degradation, following the separation of samples from the working mixture to investigate the degradation process. The catalyst In–CeO_2/g-CN was recovered by centrifugation and reused for LVX degradation under the same conditions. The percentage degradation (D) was calculated using the relation $D(\%) = (1 - C_t/C_0) \times 100$,[40] where C_t represents the LVX concentration at the specified time interval, while C_o is its initial concentration.

3. Results and discussion

3.1 Structural features

The crystal structure formation and phase purity of the synthesized materials were verified *via* XRD patterns (2θ = 10°–80°), which are shown in Fig. 2(a). The peaks present at 2θ = 28.56°, 33.16°, 47.45°, 56.34°, 59.14°, 69.53°, 76.92°, and 79.12°, corresponding to the (111), (200), (220), (311), (222), (400), (331), and (420) diffraction planes, are consistent with the standard data (00-034-0394), confirming the formation of CeO_2.[41] The indium-modified material shows a variation in its diffraction peaks, which correspond to the structural changes caused by the different ionic sizes of dopant indium and the cerium host.[42] Notably, the absence of any additional diffraction peaks for pure CeO_2 and its indium-modified composition In–CeO_2 confirms the phase purity and insertion of indium ions in the CeO_2 lattice. The lower-intensity diffraction peaks in the XRD pattern of In–CeO_2/g-CN correspond to the interaction between In–CeO_2 and g-CN, causing microstructural changes.[43,44] The distinct lattice vibrations of the synthesized materials were confirmed from the FTIR spectra, as displayed in Fig. 2(c). The presence of distinctive Ce–O and Ce–O–Ce vibrations at 460 cm^{-1} and 1052 cm^{-1} confirms the formation of the synthesized materials.[45] The peaks at 1640 cm^{-1}, 1426 cm^{-1}, 1324 cm^{-1}, and 1252 cm^{-1} in the spectra of g-CN and In–CeO_2/g-CN can be attributed to C–N heterocyclic and aromatic stretching vibrations, while the peak at 810 cm^{-1} corresponds to the bending vibration (*s*-triazine units) of the g-CN framework.[46–48] The additional –OH stretching and –OH bending observed indicate moisture adsorption on the material's surface.[49,50] The thermal TGA plots showcasing the mass loss of the material against the

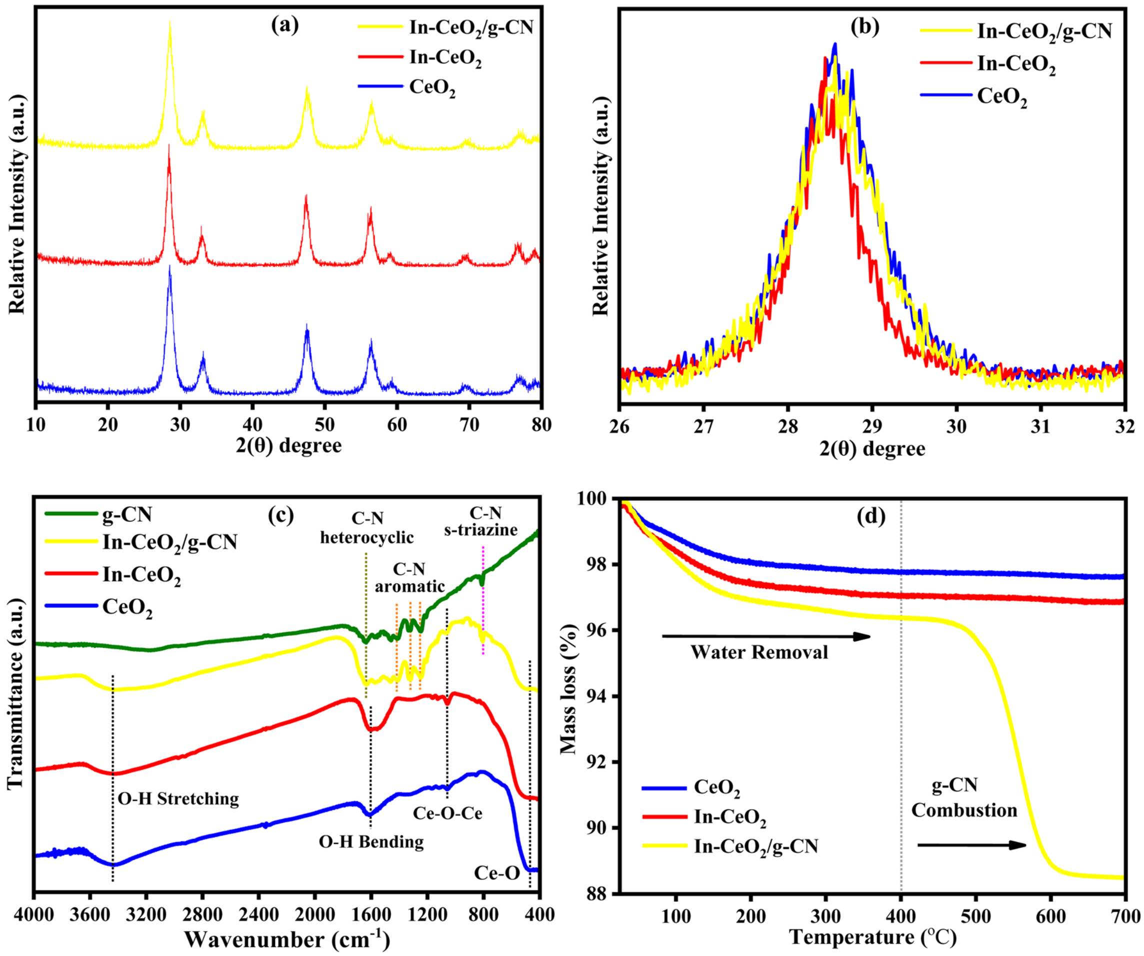

Fig. 2 (a) XRD patterns, (b) enlarged view of the diffraction patterns ($2\theta = 26–32°$), (c) FTIR spectra, and (d) TGA plots of the synthesized pure CeO_2, modified In–CeO_2, and the In–CeO_2/g-CN heterojunction.

applied temperature of CeO_2, In–CeO_2, and In–CeO_2/g-CN are shown in Fig. 2(d). In the lower temperature zone (<300 °C), minute weight losses of 2.29% (CeO_2), 3.03% (In–CeO_2), and 3.60% (In–CeO_2/g-CN) were observed, which are due to moisture removal. For the g-CN-based heterojunction material, in the higher temperature zone (400–600 °C), 7.93% of weight loss was witnessed, which corresponds to g-CN combustion.[51]

3.2 Morphological analysis

The microstructure and morphology of the synthesized CeO_2, In–CeO_2, and In–CeO_2/g-CN materials were examined by SEM analysis, and the micrographs are presented in Fig. 3. For CeO_2, a fine granular-type aggregation was observed, while for In–CeO_2, the symmetry changes to irregular-sized crystallites with varying sizes. Indium modification not only changes the microstructure from granules to crystallites, but also from aggregation to dispersion of the material. The g-CN integration further increases dispersion, preventing agglomeration, as evident in Fig. 3(d), which is substantial for photocatalytic applications.

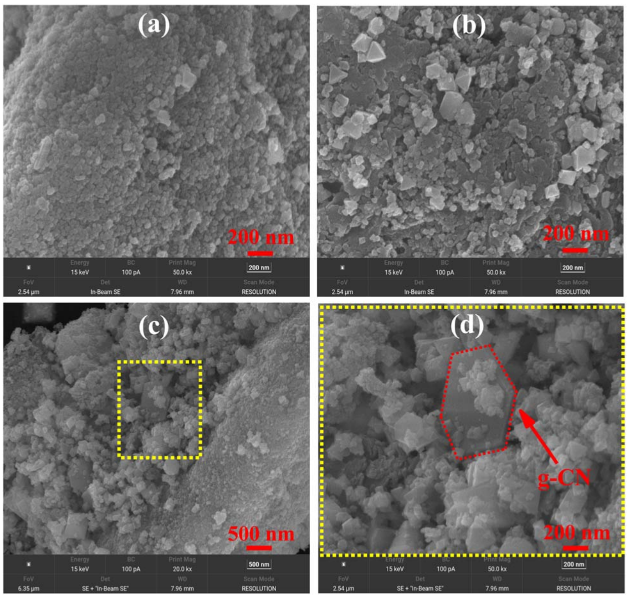

Fig. 3 SEM images of (a) CeO_2, (b) In–CeO_2, and (c and d) In–CeO_2/g-CN.

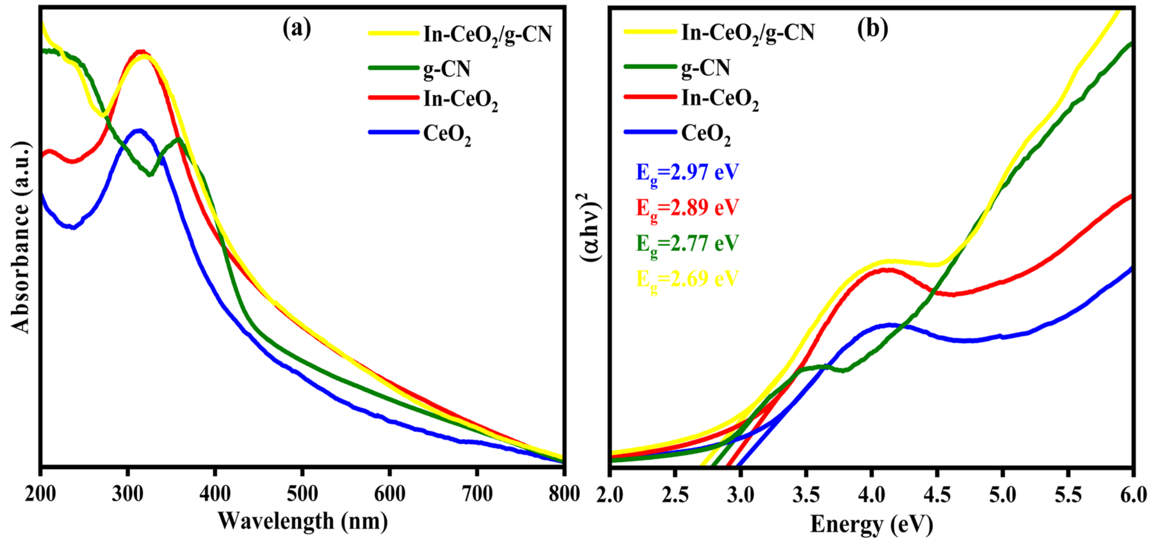

Fig. 4 (a) UV-visible absorption spectra and (b) bandgap calculation from the Tauc plot model of the synthesized CeO_2, In–CeO_2, g-CN, and In–CeO_2/g-CN.

3.3 Optical properties

The optical properties of CeO_2, In–CeO_2, g-CN, and In–CeO_2/g-CN materials were investigated by UV-vis absorption spectroscopy, and the absorption spectra observed for different materials are presented in Fig. 4(a). The synthesized materials feature absorption edges extending into the visible region. Notably, indium-modification and heterojunction formation with g-CN considerably enhances visible-light absorption, as evident from the red-shift in the absorption edge.[52,53] Fig. 4(b) presents the Tauc plots generated to calculate the optical bandgap (E_g),[54] and the materials CeO_2, In–CeO_2, g-CN, and In–CeO_2/g-CN feature an E_g of 2.97 eV, 2.89 eV, 2.77 eV, and 2.69 eV, respectively. The In–CeO_2/g-CN heterojunction (E_g = 2.69 eV) exhibits increased absorption, facilitating the separation of electron–hole pairs under visible light and rendering it promising for photocatalytic applications.

3.4 Electrochemical response

The electrochemical responses of CeO_2, In–CeO_2, g-CN, and In–CeO_2/g-CN materials were investigated to elucidate charge transfer kinetics and electron–hole recombination rates. The EIS results, presented as Nyquist plots in Fig. 5(a), reveal a distinct electrochemical response. The semicircle diameter in the Nyquist plot reflects the charge transfer resistance (R_{ct}) at the working electrode–electrolyte interface.[55] Notably, the In–CeO_2/g-CN heterojunction exhibits a smaller semicircle diameter compared to its components, g-CN and In–CeO_2, indicating lower R_{ct} and faster charge transfer kinetics.[56–58] The light-on photocurrent generation for the materials CeO_2, In–CeO_2, g-CN, and In–CeO_2/g-CN is presented in Fig. 5(b). The significantly increased photocurrent density observed for In–CeO_2/g-CN can be attributed to enhanced charge separation due to band structure alignment, which suppresses rapid electron–

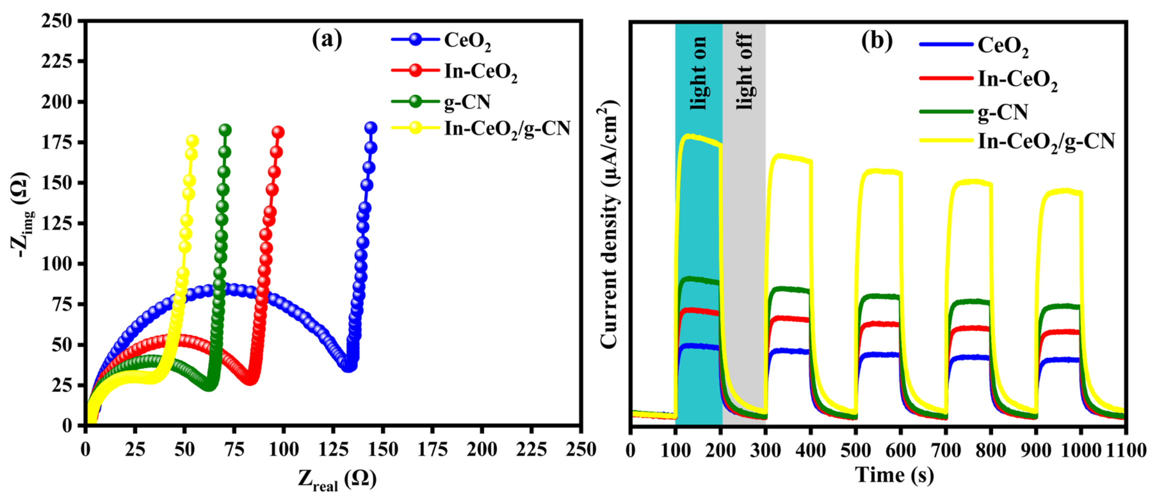

Fig. 5 (a) Nyquist plots and (b) photocurrent responses of the CeO_2, In–CeO_2, g-CN, and In–CeO_2/g-CN materials.

hole recombination.[59,60] The heterojunction formation enhances charge transport, thereby increasing the availability of electron–hole pairs or their participation in the photocatalytic process.

3.5 PC activity

The PC activity of CeO_2, In–CeO_2, and In–CeO_2/g-CN materials was estimated by degrading LVX. The UV-vis absorption data of the LVX samples separated from the aliquot at specified time intervals (in the presence of In–CeO_2/g-CN) are presented in Fig. 6(a). The absorption intensity at λ_{max} corresponds to the LVX concentration, which decreases, indicating LVX degradation. The absorption intensity rapidly declines in the presence of the photocatalyst In–CeO_2/g-CN as compared to In–CeO_2 and CeO_2, which degrade LVX to a lower extent. In Fig. 6(b), the LVX degradation (%) over the synthesized catalysts is presented, which follows the order, CeO_2 (44%) < In–CeO_2 (63%) < In–CeO_2/g-CN (85%). The order of photocatalytic efficiency is consistent with the optical properties and electrochemical responses of the photocatalysts, which feature facilitated electron–hole separation and transport in In–CeO_2/g-CN, revealing its promising potential for photocatalytic applications.

The kinetics study of LVX degradation over the photocatalysts, CeO_2, In–CeO_2, and In–CeO_2/g-CN, is shown in Fig. 7(a), which presents 1st-order kinetics for LVX degradation. The rate constants were calculated as 0.0075 min^{-1}, 0.0123 min^{-1}, and 0.0198 min^{-1}, corresponding to CeO_2, In–CeO_2, and In–CeO_2/g-CN. The scavenging study presented in Fig. 7(b) for LVX degradation in the presence of a photocatalyst with the highest photocatalytic efficacy, In–CeO_2/g-CN, was performed using EDTA, $AgNO_3$, IPA, and BQ for trapping holes (h^+), electrons (e^-), hydroxyl radicals ($HO^•$), and superoxide radicals ($^•O_2^-$), respectively. In the presence of $AgNO_3$, the decline in LVX degradation was not significant, but in the

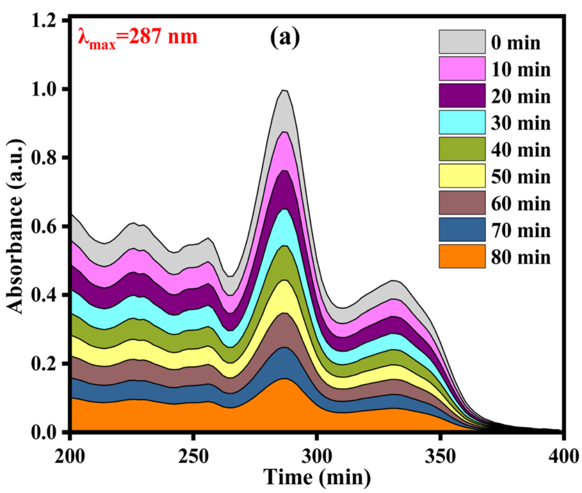

Fig. 6 (a) UV-vis absorption spectra of the samples collected during LVX degradation in the presence of In–CeO_2/g-CN and (b) comparison of the catalytic efficiency.

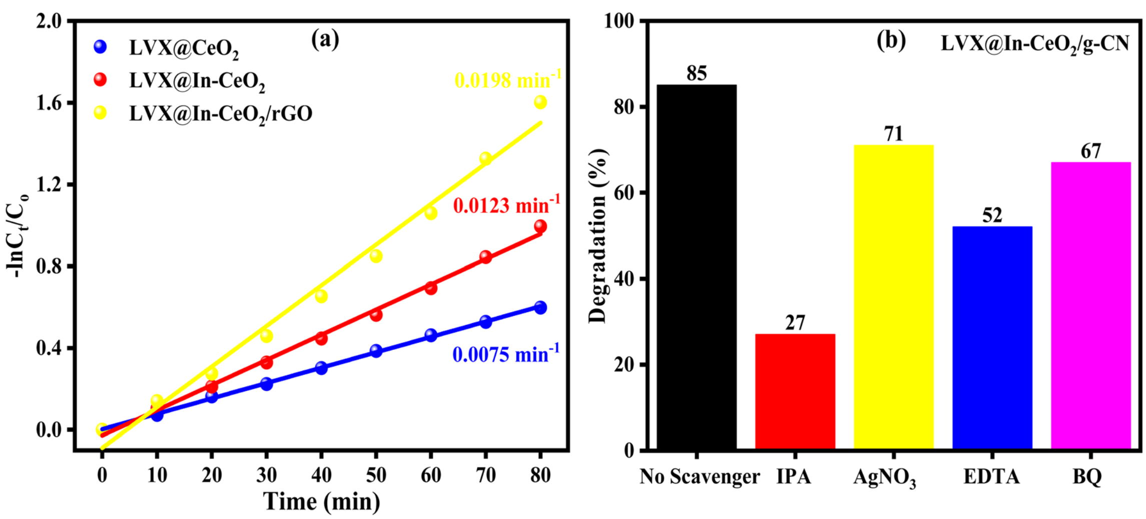

Fig. 7 (a) Kinetic studies of LVX degradation over CeO_2, In–CeO_2, and In–CeO_2/g-CN, and (b) scavenging studies over In–CeO_2/g-CN.

Table 1 Detailed comparison of the present work with previous studies

Sr. no.	Photocatalyst	Pollutant	Conditions	*D*(%)	References
1	Ag-doped g-CN/Biochar	Ciprofloxacin (CIP)	50 ppm CIP, 50 mg catalyst, visible-light, 4 h	70%	61
2	ZnO/g-CN	Methyl orange (MO)	10 ppm MO, 50 mg catalyst, 400 W lamp	83.71%	62
3	Ni-doped α-Fe_2O_3/g-CN	Ciprofloxacin (CIP)	10 mg per L CIP, 15 mg catalyst, solar light ~660 Wm^{-2}	82.1%	63
4	g-CN/$Bi_2O_2CO_3$	Carbamazepine (CBZ)	20 ppm CBZ, 1 g of catalyst, sunlight, 180 minutes	98%	64
5	$ZnCr_2O_4$/g-CN	Ciprofloxacin (CIP)	10 mg per L CIP, 75 mg of catalyst, Halogen lamp, 120 minutes	74.36%	65
6	Bi_2MoO_6/g-CN	Ciprofloxacin (CFX)	10 mg per L CFX, 0.05 g of catalyst, LED light, 90 minutes	89.04%	66
7	In–CeO_2/g-CN	Levofloxacin (LVX)	10 mg per L LVX, 50 mg catalyst, Xe lamp (300 W, UV cutoff filter λ > 420 nm), and 80 minutes	85%	Present study

presence of IPA, the degradation dropped considerably. The scavenging investigation presents the contribution of active species in the order $e^- < h^+ < {}^{\bullet}O_2^- < HO^{\bullet}$ for LVX degradation. A detailed comparison of the present work with previous findings is presented in Table 1.

Electronic band structure alignment and energy band energies hold vital significance in designing heterojunction materials with a specific scheme for charge migration. To get insights into the mechanism of LVX degradation over In–CeO_2/g-CN, the energy band values, VB maxima (E_{VB}) and CB minima

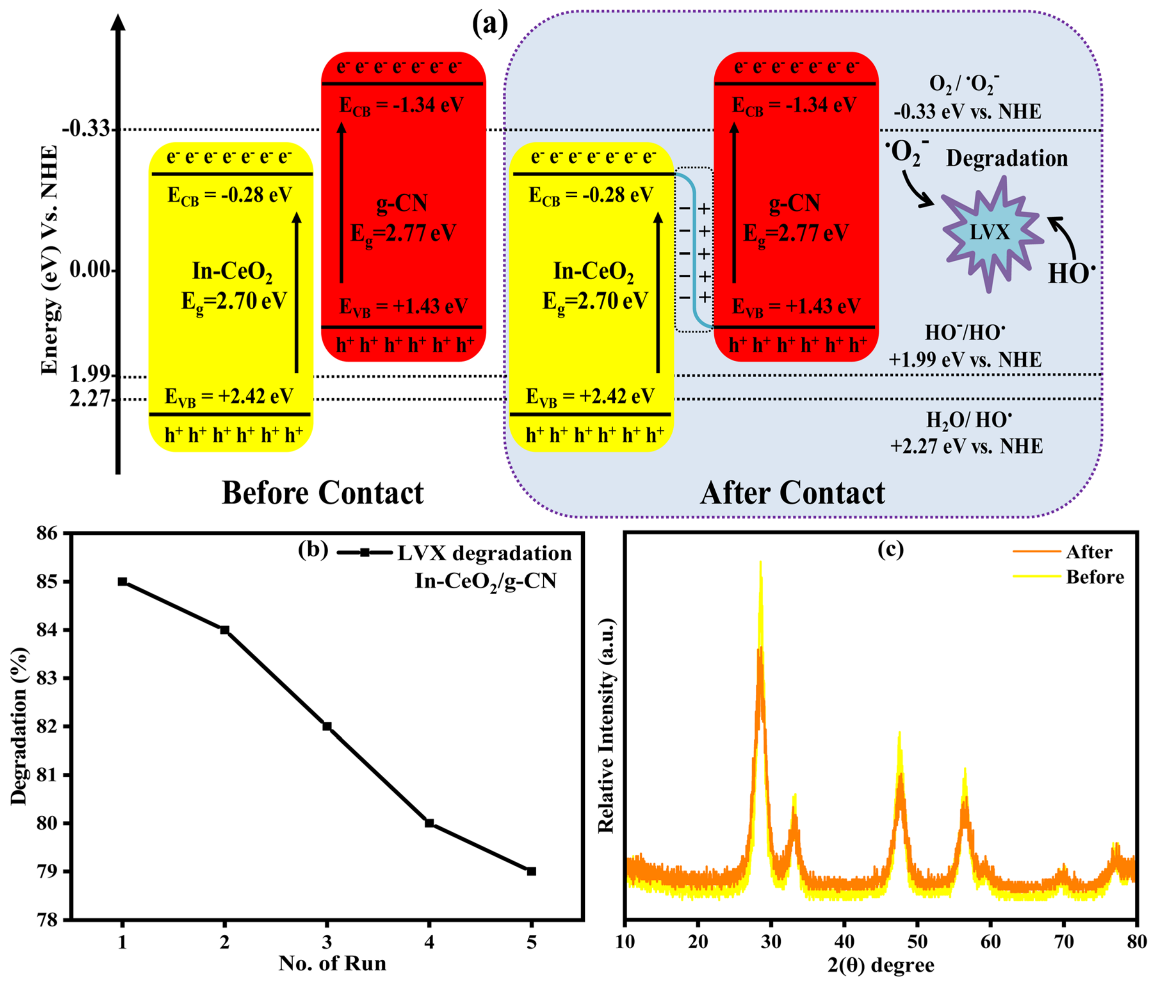

Fig. 8 (a) Schematic of the proposed S-scheme In–CeO_2/g-CN heterojunction and (b) reusability and (c) before-and-after XRD pattern alignments to study the stability of the catalyst.

(E_{CB}) of g-CN and In–CeO$_2$ were explored by applying the relations:[67,68]

$$E_{CB} = \chi - E_e - 0.5\ E_g$$

$$E_{VB} = E_{CB} + E_g$$

Here, "χ" is electronegativity, and $E_e = 4.5$ eV denotes the energy of a free electron on the hydrogen scale. The calculated energy band values were E_{VB} = +2.42 eV for In–CeO$_2$ and E_{CB} = −0.28 eV, while E_{VB} = +1.43 eV and E_{CB} = −1.34 eV for g-CN. Thermodynamically, pure In–CeO$_2$ is unable to generate $^{\bullet}O_2^-$ radicals due to E_{CB} being higher than the required reduction potential ($O_2/^{\bullet}O_2^-$ = −0.33 eV *vs.* NHE,[69]). Pure g-CN is unable to generate $HO^{\bullet}$ radicals as it has an E_{VB} value lower than the required oxidation potential ($HO^-/HO^{\bullet}$ = 1.99 eV and $H_2O/HO^{\bullet}$ = 2.23 eV *vs.* NHE,[70]). But the scavenging studies reveal the generation of both $^{\bullet}O_2^-$ and $HO^{\bullet}$ radicals, which degrade LVX. As shown in (Fig. 8), the low-redox-potential carriers, e^- of In–CeO$_2$ and h^+ of g-CN, recombine, leaving behind the active e^- (g-CN) and h^+ (In–CeO$_2$),[71,72] which participate in the reduction and oxidation reactions producing active radical species that degrade LVX.

The reusability and structural stability of In–CeO$_2$/g-CN were studied by LVX degradation in different runs, and the results are presented in Fig. 8(b and c). The photocatalyst retains ∼95% of its initial activity after multiple cycles, indicating good structural stability and recyclability; minor losses are likely due to insufficient catalyst recovery. The diffraction pattern of the recovered catalyst displays its structural stability, as no significant change was detected.

4. Conclusion

Pure CeO$_2$ and its indium-modified composition, In–CeO$_2$, were hydrothermally fabricated, while g-CN was synthesized through melamine calcination. The In–CeO$_2$ material was dispersed on g-CN through ultrasonication to construct the S-scheme In–CeO$_2$/g-CN heterojunction. XRD and FTIR analyses verified the formation of CeO$_2$, In–CeO$_2$, and In–CeO$_2$/g-CN, with thermal stability indicated by TGA. SEM micrographs showcased the dispersion of In–CeO$_2$, with g-CN preventing agglomeration. The In–CeO$_2$/g-CN heterojunction increased visible-light absorption under λ > 420 nm illumination and facilitated charge separation *via* band structure alignment, forming an S-scheme of charge migration. The PC efficiency was evaluated by LVX degradation in the presence of catalysts, CeO$_2$, In–CeO$_2$, and In–CeO$_2$/g-CN. The In–CeO$_2$/g-CN catalyst exhibited a maximum LVX degradation of 85% (0.0198 min^{-1}) compared to CeO$_2$ and In–CeO$_2$, which degraded LVX to an extent of 44% (0.0075 min^{-1}) and 63% (0.0123 min^{-1}), respectively. The formation of the In–CeO$_2$/g-CN S-scheme heterojunction enables the recombination of low-redox-potential charge carriers (with low redox ability), preventing active charge carriers (high redox ability) from recombining and making them available for photocatalytic reactions. Despite the improved activity, the study is limited to a single pollutant and Xe-lamp illumination conditions; future work will evaluate performance under solar-simulated visible light and conduct advanced interfacial analyses such as XPS.

Author contributions

Mazen R. Alrahili (writing – original draft, validation), M. Abdel Rafea (funding acquisition, project administration, resources), Magdi E. A. Zaki (investigation, formal analysis), M. Khairy (data curation, validation), Mohamed. R. El-Aassar (investigation, data curation), Sultan Albarakati (software, methodology), Imran Shakir (visualization, formal analysis), Abdullah K. Alanazi (writing – review & editing), Muhammad Aadil (supervision).

Conflicts of interest

There are no conflicts to declare.

Data availability

Data will be available upon request.

Acknowledgements

This work was supported and funded by the Deanship of Scientific Research at Imam Mohammad Ibn Saud Islamic University (IMSIU) (grant number IMSIU-DDRSP2502).

References

1 J. Zhang, X. Wang, X. Wang and C. Li, Heterophase junction effect on photogenerated charge separation in photocatalysis and photoelectrocatalysis, *Acc. Chem. Res.*, 2025, **58**, 787–798.
2 P. Swaminaathan, A. Saravanan, P. Yaashikaa and A. Vickram, Recent advances in photocatalytic degradation of persistent organic pollutants: Mechanisms, challenges, and modification strategies, *Sustain. Chem. Environ.*, 2024, **8**, 100171.
3 Y. Sari, P. L. Gareso, B. Armynah and D. Tahir, A review of TiO2 photocatalyst for organic degradation and sustainable hydrogen energy production, *Int. J. Hydrogen Energy*, 2024, **55**, 984–996.
4 M.-A. Gatou, A. Syrrakou, N. Lagopati and E. A. Pavlatou, Photocatalytic TiO2-based nanostructures as a promising material for diverse environmental applications: a review, *Reactions*, 2024, **5**, 135–194.
5 A. R. Bhapkar and S. Bhame, A review on ZnO and its modifications for photocatalytic degradation of prominent textile effluents: Synthesis, mechanisms, and future directions, *J. Environ. Chem. Eng.*, 2024, **12**, 112553.
6 N. T. T. Nguyen, A. N. Q. Phan, T. Van Tran and T. T. T. Nguyen, Morinda citrifolia fruit extract-mediated synthesis of ZnO and Ag/ZnO nanoparticles for photocatalytic degradation of tetracycline, *Environ. Res.*, 2025, **273**, 121209.

7 L. D. Sonawane, A. S. Mandawade, L. N. Bhoye, H. I. Ahemad, S. S. Tayade, Y. B. Aher, A. B. Gite, L. K. Nikam, S. D. Shinde and G. H. Jain, Sol-gel and hydrothermal synthesis of CeO2 NPs: their physiochemical properties and applications for gas sensor with photocatalytic activities, *Inorg. Chem. Commun.*, 2024, **164**, 112313.

8 K. Sharma, S. Sonu, A. Sudhaik, T. Ahamad, S. Kaya, S. Thakur, Q. Van Le, V.-H. Nguyen, A. Singh and L. H. Nguyen, Mechanistic insights into the reaction pathway for efficient cationic dye photocatalytic degradation and the importance of the enhanced charge isolation over dual Z-scheme CeO2/BiOCl/Ag2WO4 photocatalyst, *J. Water Proc. Eng.*, 2024, **66**, 105918.

9 J. Wang, X. Niu, Q. Hao, K. Zhang, X. Shi, L. Yang, H. Y. Yang, J. Ye and Y. Wu, Promoting charge separation in CuInS2/CeO2 photocatalysts by an S-scheme heterojunction for enhanced photocatalytic H2 production, *Chem. Eng. J.*, 2024, **493**, 152534.

10 M. N. Shabbir, R. Alabada, M. Aadil, Z. Ahmad, A. A. Alothman, N. A. Almuhous, W. A. Khan and R. M. Mohamed, Synthesis, structural characterizations, and photocatalytic application of silver-doped indium oxide ceramic nanoparticles, *Ceram. Int.*, 2024, **50**, 4404–4414.

11 M. A. Hamza, A. El-Sayed, A. N. El-Shazly and M. G. Elmahgary, Efficient utilization of ceramic waste (cyclone dust waste) for enhancing the photocatalytic performance of TiO2 nanoparticles toward Rhodamine B photodegradation, *J. Cleaner Prod.*, 2024, **434**, 140341.

12 L. Al-Hajji, A. Al-Anazi, A. A. Ismail, A. M. El-Toni, A. Khan and M. Shkir, A pn heterojunction PdO/CeO2 photocatalysts with enhanced photocatalytic ability for reduction of Hg (II) ions from aqueous solution, *Ceram. Int.*, 2024, **50**, 45650–45657.

13 A. Rianjanu, K. D. P. Marpaung, C. Siburian, S. A. Muhtar, N. I. Khamidy, J. Widakdo, N. Yulianto, R. Aflaha, K. Triyana and T. Taher, Enhancement of photocatalytic activity of CeO2 nanorods through lanthanum doping (La–CeO2) for the degradation of Congo red dyes, *Results Eng.*, 2024, **23**, 102748.

14 S. R. A. Kumar, D. V. Mary, G. S. Josephine and A. Sivasamy, Hydrothermally synthesized WO3: CeO2 supported gC3N4 nanolayers for rapid photocatalytic degradation of azo dye under natural sunlight, *Inorg. Chem. Commun.*, 2024, **164**, 112366.

15 D. Yang, Q. Ye, C. Qu, F. Meng, L. Wang and Y. Li, Enhanced hydrogen evolution and tetracycline degradation by a Z-scheme g-C3N4 nanosheets loaded CeO2 photocatalyst under visible light irradiation, *J. Environ. Chem. Eng.*, 2024, **12**, 112563.

16 H. Zhang, L. Bao, Y. Pan, J. Du and W. Wang, Interface reconstruction of MXene-Ti3C2 doped CeO2 nanorods for remarked photocatalytic ammonia synthesis, *J. Colloid Interface Sci.*, 2024, **675**, 130–138.

17 M. C. Iannaco, S. Mottola, V. Vaiano, G. Iervolino and I. De Marco, CeO2-CuO composites prepared via supercritical antisolvent precipitation for photocatalytic hydrogen production from lactic acid aqueous solution, *J. CO_2 Util.*, 2024, **85**, 102878.

18 Fauzia, M. A. Khan, M. Chaman and A. Azam, Antibacterial and sunlight-driven photocatalytic activity of graphene oxide conjugated CeO2 nanoparticles, *Sci. Rep.*, 2024, **14**, 6606.

19 J. Naseem, M. A. Rafea, M. E. A. Zaki, M. I. Attia, M. R. El-Aassar, F. Alresheedi, S. Zulfiqar and M. Aadil, Combining nanotechnology and nanohybrid methods to improve the physical and chemical properties of CuS and boost its photocatalytic aptitude, *RSC Adv.*, 2025, **15**, 13940–13950.

20 S. Ali, H. Ali, S. H. Bakhtiar, S. Ali, M. Zahid, A. Ismail, P. M. Ismail, A. Zada, I. Khan and H. Shen, Bifunctional phosphate-modulated Cu2O/CeO2 redox heterojunction: a promising approach for proficient CO2 reduction, *J. Alloys Compd.*, 2024, **972**, 172766.

21 V. Rajappa, S. Mohan, S. Bharathkumar, S. L. Rokhum, A. Fatehmulla, H. Valdes and R. Ilangovan, Fe, N Dual-Doped Cerium Oxide Photocatalyst Manifesting the Simultaneous Degradation of Dye–Heavy Metal Mixed Pollutants under Sunlight, *Ind. Eng. Chem. Res.*, 2024, **63**, 21760–21770.

22 L. Luo, R. Wang, T. Wang, J. Li, Y. Xiao, K. Qi, X. Guo, Z. Feng, J. Tang and F. Zhang, Coverage-Dependent Selective Conversion of Methane into Value-Added Ethane over Noble-Metal-Free Ni1-CeO2 Photocatalyst, *J. Am. Chem. Soc.*, 2025, **147**, 17566–17573.

23 Q. Liu, G. Tan, Y. Long, J. Wei, H. Tian, S. Xie and Y. Tang, In situ formation of CeO 2 coupled with hollow NiCo-LDH nanosheets for efficient photocatalytic hydrogen evolution, *Inorg. Chem. Front.*, 2024, **11**, 5080–5090.

24 A. Balapure, J. R. Dutta and R. Ganesan, Recent advances in semiconductor heterojunctions: a detailed review of the fundamentals of photocatalysis, charge transfer mechanism and materials, *RSC Appl. Interfaces*, 2024, **1**, 43–69.

25 Y. Liu, M. Li, T. Liu, Z. Wu and L. Zhang, Enhanced charge carrier transport in TiO2/COF S-scheme heterojunction for efficient photocatalytic H2O2 production, *J. Mater. Sci. Technol.*, 2025, **233**, 201–209.

26 R. Kumar, A. Sudhaik, D. Kumar, R. Devi, E. Devi, A. Chawla, P. Raizada, C. M. Hussain, T. Ahamad and P. Singh, Synergistic photocatalytic activity of Bi2O3/g-C3N4/ZnO ternary heterojunction with dual Z-scheme charge transfer towards textile dye degradation, *J. Ind. Eng. Chem.*, 2025, **144**, 575–584.

27 H. Sun, L. Wang, X. Wang, Y. Dong, J. Ren, J. Xin, R. Jing and J. An, A novel WO3/ZnIn2S4/CoWO4 heterojunction for enhancement of photocatalytic degradation sparfloxacin: Dual S-scheme multi-charge transfer mode and Mechanistic pathway, *J. Environ. Chem. Eng.*, 2024, **12**, 112386.

28 Y.-H. Wu, Y.-Q. Yan, Y.-X. Deng, W.-Y. Huang, K. Yang and K.-Q. Lu, Rational construction of S-scheme CdS quantum dots/In2O3 hollow nanotubes heterojunction for enhanced photocatalytic H2 evolution, *Chin. J. Catal.*, 2025, **70**, 333–340.

29 G. Arulprakash and R. Vijayaraghavan, Charge-separated 3D/2D layered heterojunction of NiNb2O6/E-gC3N4 as an efficient photocatalyst for photo-reduction of Cr6+ and photo-oxidation of dyes under visible and sunlight, *Appl. Surf. Sci.*, 2025, **684**, 161938.

30 M. Bilal, M. Q. Alfaifi, S. B. Ahmed, M. M. Abduljawad, Y. I. Alrashed, E. S. Aldurahim and Y. A. Alassmy, A review of strategies to switch heterojunction system from type-II to S-scheme for photocatalytic applications, *Mater. Sci. Semicond. Process.*, 2025, **186**, 109051.

31 B. Zhu, J. Sun, Y. Zhao, L. Zhang and J. Yu, Construction of 2D S-scheme heterojunction photocatalyst, *Adv. Mater.*, 2024, **36**, 2310600.

32 M. Aldrdery, F. Alresheedi, M. R. El-Aassar, A. Ahmed, M. Aadil, A. Alazmi, A. El Jery, M. R. Alrahili and A. Amjad, Preparation and physicochemical characterization of highly efficient ZrO2/g-C3N4 composite catalysts for visible-light-driven removal of tetracycline antibiotics, *Diamond Relat. Mater.*, 2025, **151**, 111801.

33 A. Majeed, S. Hassan, M. Zahra, I. Rafique, S. Iqbal, M. A. Shafiq, R. N. Qureshi, R. Akhtar, M. Rehan and M. A. R. Anjum, Mechanistic insights into the visible light photocatalytic activity of gC 3 N 4/Bi 2 O 2 CO 3–Bi 4 O 7 composites for rhodamine B degradation and hexavalent chromium reduction, *RSC Adv.*, 2025, **15**, 16643–16653.

34 M. R. El-Aassar, H. M. A. Hassan, M. S. Alhumaimess, I. H. Alsohaimi, M. Alzaid, A. K. Alanazi, M. Algarni, S. Albarakati and M. Aadil, Synthesis of Nd/Ni co-doped $LaFeO_3$/g-C_3N_4 heterostructures for photocatalytic norfloxacin degradation, *Inorg. Chem. Commun.*, 2025, **182**, 115478.

35 A. Gandamalla, S. Manchala, P. Anand, Y.-P. Fu and V. Shanker, Development of versatile CdMoO4/g-C3N4 nanocomposite for enhanced photoelectrochemical oxygen evolution reaction and photocatalytic dye degradation applications, *Mater. Today Chem.*, 2021, **19**, 100392.

36 P. Panchal, P. Rauwel, S. Sharma, S. Nehra, E. Estephan, K. Praakle, E. Rauwel, *Bio-Synthesis of Graphitic Carbon Nitride and ZnO/GCN Nanohybrid for Remarkable Environmental Application*, 2024.

37 G. Karthik, S. Mohan and R. G. Balakrishna, Ligand modulated charge transfers in Z-scheme configured Ni-MOF/g-C3N4 nanocomposites for photocatalytic remediation of dye-polluted water, *Sci. Rep.*, 2024, **14**, 26149.

38 A. Gandamalla, S. Manchala, A. Verma, Y.-P. Fu and V. Shanker, Microwave-assisted synthesis of ZnAl-LDH/g-C3N4 composite for degradation of antibiotic ciprofloxacin under visible-light illumination, *Chemosphere*, 2021, **283**, 131182.

39 K. M. Katubi, S. Jabeen, F. Tariq, A. Irshad, Z. Alrowaili, M. Al-Buriahi and M. F. Warsi, Harnessing advanced nanomaterials: wastewater treatment with sustainable approach using 2D g-C3N4 based Ho-doped LaCoO3 nanocomposite, *Ceram. Int.*, 2024, **50**, 12415–12426.

40 K. Shafiq, M. Aadil, W. Hassan, Q. Choudhry, S. Gul, A. Rais, A. A. Fattah, K. H. Mahmoud and M. Z. Ansari, Cobalt and holmium co-doped nickel ferrite nanoparticles: synthesis, characterization and photocatalytic application studies, *Z. Phys. Chem.*, 2023, **237**, 1325–1344.

41 H. I. Ahemad, G. E. Patil, Y. B. Aher, M. S. Malik, L. D. Sonawane, M. A. More, A. S. Mandawade, D. Y. Patil, S. D. Shinde and G. H. Jain, Synthesis and characterization of CeO2 nanoparticles using Plectranthus barbatus leaf extract and its CO gas sensing and antimicrobial activity, *Mater. Lett.*, 2025, **379**, 137652.

42 K. M. Katubi, A. Rasheed, A. Ihsan, B. Shaheen, Z. Alrowaili, M. Al-Buriahi, M. I. Din, I. Shakir and S. Munir, Neodymium-doped nickel cobaltite reinforced with 2D MXene nanocomposite (Nd-NiCo2O4/MXene) for enhanced photocatalytic degradation of the organic pollutants, *Opt. Mater.*, 2024, **152**, 115390.

43 X. Yu, X. Tang, H. Luo and Y. Mao, Construction of biochar assisted S-scheme of CeO2/g-C3N4 with enhanced photoreduction CO2 to CO activity and selectivity, *Mater. Res. Bull.*, 2025, **181**, 113085.

44 H. Somaily, Construction of g-CN/SnSe nanocomposite through a hydrothermal approach for enhanced OER study, *Ceram. Int.*, 2024, **50**, 33382–33391.

45 T. Fei, Performance and mechanism of constructed CuO/CeO2 p–n heterojunction for photocatalytic degradation of methylene blue, *Trans. Nonferrous Met. Soc. China*, 2024, **34**, 1951–1964.

46 N. M. Ghazy, E. A. Ghaith, Y. Abou El-Reash, R. R. Zaky, W. M. Abou El-Maaty and F. S. Awad, Enhanced performance of hydroxyl and cyano group functionalized graphitic carbon nitride for efficient removal of crystal violet and methylene blue from wastewater, *RSC Adv.*, 2022, **12**, 35587–35597.

47 M. E. Ali, M. Abouelfadl, N. A. Badway and K. M. Salam, Effective removal of organic compounds using a novel cellulose acetate coated by PA/g-CN/Ag nanocomposite membranes, *Surf. Interfaces*, 2022, **29**, 101748.

48 A. Baishnisha, K. Divakaran, V. Balakumar, K. N. Perumal, C. Meenakshi and R. S. Kannan, Synthesis of highly efficient g-CN@ CuO nanocomposite for photocatalytic degradation of phenol under visible light, *J. Alloys Compd.*, 2021, **886**, 161167.

49 N. AlMasoud, A. Irshad, U. Rafiq, T. S. Alomar, A. A. Al-wallan, M. F. Warsi and Z. M. El-Bahy, Sol-gel synthesis of Tb-doped lithium-nickel ferrite anchored onto g-C3N4 sheets for efficient photocatalytic degradation of organic dyes, *Ceram. Int.*, 2024, **50**, 46892–46903.

50 M. Yusuf, F. M. Elfghi, S. A. Zaidi, E. C. Abdullah and M. A. Khan, Applications of graphene and its derivatives as an adsorbent for heavy metal and dye removal: a systematic and comprehensive overview, *RSC Adv.*, 2015, **5**, 50392–50420.

51 B. Huwaimel, K. M. Younes, A. S. Abouzied, S. A. Almahmoud, S. Alshehri, Z. M. El-Bahy and M. F. Warsi, Cerium-doped indium vanadate microspheres loaded onto the 2D conductive matrix for boosted photodegradation of persistent organic pollutants, *Ceram. Int.*, 2025, **51**, 12806–12817.

52 M. F. Abou Taleb and M. M. Ibrahim, Indium-doped tungsten oxide architectures anchored on 2D rGO Matrix with enhanced visible-light-response and efficient charge separation for photocatalytic degradation of organic pollutants, *J. Alloys Compd.*, 2024, **1003**, 175628.

53 L. Xu, P. Guo, J. Xu, B. Shen and Z. Zhao, Regulation of TiO2/ZSM-5 catalyst for enhanced photocatalytic toluene oxidation: Intensified light absorption, charge separation and toluene adsorption, *Colloids Surf., A*, 2024, **690**, 133832.

54 A. Rasheed, I. Bibi, F. Majid, S. Kamal, B. Taj, M. Raza, N. Khaliq, K. M. Katubi, S. Ezzine and N. Alwadai, Mn doped SrFe12O19 fabricated via facile microemulsion route and solar-light-driven photocatalytic removal of crystal violet dye, *Phys. B*, 2022, **646**, 414303.

55 S. Baqi, M. T. Oo and F. C. C. Ling, Unveiling the impact of Cu doping on charge carrier density and transfer in ZnO/ZnSe heterojunctions for PEC applications, *Mater. Sci. Semicond. Process.*, 2025, **198**, 109780.

56 K. Kalidasan, S. Mallapur and S. G. Kumar, Pivotal role of surface and bulk Gd species in WO3 to promote Type-II charge carrier transfer pathways in Gd-WO3/g-C3N4 heterojunction photocatalyst, *J. Environ. Chem. Eng.*, 2024, **12**, 113054.

57 K. K. Das, U. A. Mohanty, R. Mohanty, P. P. Sarangi, D. P. Sahoo and K. Parida, Improving charge carrier separation through S-scheme-based 2D–2D WS2/sulfur-doped g-C3N4 heterojunctions for a superior photocatalytic O2 reduction reaction, *ACS Appl. Energy Mater.*, 2024, **7**, 6360–6375.

58 M. Yi, Y. Ren, X. Zhang, Z. Zhu and J. Zhang, Ionic liquid-assisted synthesis of N, F, and B co-doped BiOBr/Bi2Se3 on Mo2CTx for enhanced performance in hydrogen evolution reaction and supercapacitors, *J. Colloid Interface Sci.*, 2024, **658**, 334–342.

59 L. Shuai, L. Tian, X. Huang, J. Dou, J. Yu and X. Chen, Enhanced charge carrier separation and stable photoelectrochemical water splitting via a high-performance BiVO4/BiOBr Type-II heterojunction, *Int. J. Hydrogen Energy*, 2024, **88**, 19–28.

60 G. Zheng, S. Jiang, M. Cai, F. Zhang and H. Yu, WO3/FeOOH heterojunction for improved charge carrier separation and efficient photoelectrochemical water splitting, *J. Alloys Compd.*, 2024, **981**, 173637.

61 I. Idrees, M. Zafar, M. A. Umer, F. Rehman, A. Razzaq, S. Kim, Y. Yang and W. Y. Kim, Silver (Ag) doped graphitic carbon nitride (g-C3N4)/biochar composite photocatalyst for improved photocatalytic degradation of ciprofloxacin (CIP), *Results Phys.*, 2025, **68**, 108071.

62 A. H. Warda, M. Rostom, M. I. Mashaly, E. T. Helmy, E. A. Gomaa and E. M. AbouElleef, Facile and eco-friendly synthesis of GCN/ZnO nanocomposites for enhanced photocatalytic, antimicrobial and antioxidant activities: applications in biomedicine and wastewater treatment, *Surf. Interfaces*, 2025, 107123.

63 C. N. Lakshmi, M. Irfan, R. Sinha and N. Singh, Magnetically recoverable Ni-doped iron oxide/graphitic carbon nitride nanocomposites for the improved photocatalytic degradation of ciprofloxacin: Investigation of degradation pathways, *Environ. Res.*, 2024, **242**, 117812.

64 J. U. R. Abbasi, K. H. Leong, L. C. Sim, C. Dai, A. A. Aziz, S. Sethupathi and S. Ibrahim, Amalgamation of g-C3N4/Bi2O2CO3 heterojunction composites for enhanced sunlight photocatalytic removal of carbamazepine, *Environ. Sci. Pollut. Res.*, 2025, 1–14.

65 R. R. Chandrapal, K. Bharathi, G. Bakiyaraj, S. Bharathkumar, Y. Priyajanani, S. Manivannan, J. Archana and M. Navaneethan, Harnessing ZnCr2O4/g-C3N4 nanosheet heterojunction for enhanced photocatalytic degradation of rhodamine B and ciprofloxacin, *Chemosphere*, 2024, **350**, 141094.

66 P. T. Le, T. P. Nguyen, H. N. Nguyen, T. H. Tran, T. H. Do, P. T. Thuy, T. M. T. Dinh, T. Tsubota, V. D. Nguyen and T. D. Nguyen, Z-scheme Bi2MoO6/g-C3N4 heterojunction for efficient antibiotic degradation via persulfate activation under visible light, *Water Sci. Eng.*, 2025, **18**(4), 515–526.

67 P. Vijayarengan, S. C. Panchangam, A. Stephen, G. Bernatsha, G. K. Murali, S. S. Loka, S. K. Manoharan, V. Vemula, R. R. Karri and G. Ravindran, Highly efficient visible light active iron oxide-based photocatalysts for both hydrogen production and dye degradation, *Sci. Rep.*, 2024, **14**, 18299.

68 L. Zhao, J. Li, J. Shao, L. Zhang, Y. Ji, X. Li and D. Ju, Antimicrobial studies of visible light-responsive nanoflower spheres Bi2WO6/ZnO, *Ceram. Int.*, 2024, **50**, 48948–48966.

69 W. Miao, W. He, L. Shen, Y. Li, Z. Fang, Z. Yang and G. Kai, Nitrogen-oxygen defect engineering enhanced intrinsic electric field in CoFe2O4/g-C3N4 heterojunctions for photocatalytic tetracycline degradation and H2 evolution, *J. Environ. Chem. Eng.*, 2024, **12**, 114202.

70 Q. Wang, C. Yao, X. Liu, J. Qiu, R. Wang, J. Liu and W. Wang, 1D rod-like {220}-faceted CeO 2/ZnO S-scheme heterojunctions: design, photocatalytic mechanism and DFT calculations, *J. Mater. Chem. A*, 2024, **12**, 24441–24458.

71 L. Zhang, J. Zhang, J. Yu and H. García, Charge-transfer dynamics in S-scheme photocatalyst, *Nat. Rev. Chem.*, 2025, 1–15.

72 M. Gu, Y. Yang, B. Cheng, L. Zhang, P. Xiao and T. Chen, Unveiling product selectivity in S-scheme heterojunctions: Harnessing charge separation for tailored photocatalytic oxidation, *Chin. J. Catal.*, 2024, **59**, 185–194.